# Acoustic phonon softening enhances phonon scattering in Zintl-phase II-I-V compounds

Shao-Fei Wang [1,2,3] Jun-Rong Zhang,[1,2,3,*] and Fang-Wei Wang [2,3,4,5,†]

[1]*Institute of High Energy Physics, Chinese Academy of Sciences, Beijing 100049, China*
[2]*Spallation Neutron Source Science Center (SNSSC), Dongguan 523808, China*
[3]*School of Nuclear Sciences and Technology, University of Chinese Academy of Sciences, Beijing 100049, China*
[4]*Beijing National Laboratory for Condensed Matter Physics, Institute of Physics,*
*Chinese Academy of Sciences (CAS), Beijing 100080, China*
[5]*Songshan Lake Material Laboratory, Dongguan, Guangdong 523808, China*

The thermoelectric properties of nine Zintl-phase semiconductors II-I-V (II = Ca, Sr, Ba, I = Cu, Ag, Au, and V = As, Sb, Bi) are studied by using first-principles calculations. The electronic and thermal transport properties are calculated to elucidate the thermoelectric performance. The electron localization functions and crystal orbital Hamilton population show regular and anisotropic bonding in II-I-V, which makes anisotropic thermal and electronic transport properties. The phonon dispersion curve also shows element dependent distributions. We suggest that the regularity of phonon and electron distribution makes the adjusting of thermoelectric performance in $P6_3/mmc$ type Zintl-phase compounds possible. The mix of ionic and weak covalent bonding leads to the coexistence of soft phonon modes and favorable electronic properties and thus a high figure of merit (0.41–0.94). We also investigate the three phonon scattering properties. The importance of acoustic phonon softening in lowering thermal conductivity is observed. The symmetry-based three-phonon scattering pathways demonstrate the possible intense phonon-phonon scattering. These data provide a deep understanding of the thermoelectric properties in Zintl-phase compounds.

## I. INTRODUCTION

Thermoelectric materials [1] have been a topic of intensive research [2–5], for they can transform waste heat into usable power [6,7]. The electrical current is produced by thermoelectric material under the thermal voltage, which is driven by the thermal gradient [1]. Low thermal conductivity $\kappa$ is important to preserve the thermal gradient. $\kappa$ contains the electrical $\kappa_e$ and lattice $\kappa_{lat}$ components. Materials with low $\kappa$ and favorable electronic transport properties will have efficient thermoelectric performance. However, it is hard to optimize both the electronic and thermal transport properties, for the electronic part is connected to the electronic transport. Suppressing the $\kappa_{lat}$ becomes an effective way to fabricate high-performance thermoelectric materials.

In semiconductors, phonon is an important quasiparticle that dominates $\kappa_{lat}$. Materials with intense phonon scattering and strong phonon anharmonicity have low $\kappa_{lat}$ [6]. Investigating the phonon propagation gives insight into the thermal transport properties. Designing defects in materials can intensify the phonon scattering by inducing a phonon scattering center [8,9] and nanostructure can induce the boundary scattering. However, suppressing $\kappa_{lat}$ runs the risk of degrading the thermoelectric power factor (PF, PF $= S^2\sigma$) [10]. Thus designing materials with intrinsically low $\kappa_{lat}$ is the priority.

Zintl phase compounds with "electron-crystal" electronic structure and "phonon glass" have been thought of as the promising thermoelectric materials. The complex crystals and covalent bonding [11] result in low $\kappa$ and high Seebeck coefficients. Several Zintl-phase compounds have been synthesized with efficient thermoelectric performance, such as $YbMg_2Sb_2$ [12] and $Eu_2ZnSb_2$ [13]. Designing new Zintl-phase materials with promising thermoelectric applications is still desirable. Chemical replacements are efficient strategies for designing novel materials with functional applications [14,15]. Several $n$-type Zintl-phase compounds with desirable thermoelectric performance have been proposed by chemical replacement methods [14]. 8-electron and 18-electron half-Heusler compounds [16] are widely studied for energy conversion applications, but the 8-electron Zintl-phase compounds need to be explored.

Based on the crystal structure of BaAgSb, nine 8-electron Zintl-phase semiconductors II-I-V (II = Cu, Sr, Ba, I = Cu, Ag, Au, and V = As, Sb, Bi) with intrinsically low $\kappa_{lat}$ are proposed. The mechanical and thermodynamical stability are analyzed via the elastic constants and molecular dynamical simulations. The anisotropic thermoelectric performance of II-I-V is systematically investigated. The detailed crystal structure, electronic band structure, electronic transport properties, and phonon transport properties are investigated. The temperature, momentum, and band dependent carrier lifetimes are estimated by considering the electron-phonon scattering near the Fermi level. The phonon anharmonicity and three phonon transport properties are calculated to illustrate the

*Corresponding author: jrzhang@ihep.ac.cn
†Corresponding author: fwwang@iphy.ac.cn

ultralow $\kappa_{\text{lat}}$. The possible three phonon scattering channels are calculated to illustrate the intense phonon scattering in the $P6_3/mmc$ crystal. Finally, the thermoelectric performance of Zintl phase II-I-V is calculated, which demonstrates promising thermoelectric application. According to our calculations, the characteristics and regularity in the hexagonal Zintl-phase compounds are summarized, which will give insights into the experiments and motivate future research.

## II. CALCULATION METHODS

Density function theory (DFT) based on the plane-wave projector augmented wave method in the Vienna *ab initio* simulation package (VASP) [17] is used in the calculation of II-I-V. All the simulations are carried out by the projector-augmented wave (PAW) potentials [18] with the plane wave energy up to 650 eV. The generalized gradient approximation (GGA) with the Perdew-Burke-Ernzerhof (PBE) [19] parametrization is chosen for the exchange-correlation energy functional. The energy convergence criterion of the electron self-consistency is set to $10^{-7}$ eV. A Monkhorst-Pack $6 \times 6 \times 4$ **k** mesh is used for the structure optimizations. These crystals are fully optimized until the Hellman-Feynman force is less than $0.001$ eV $\text{\AA}^{-1}$. The electronic band structures are calculated using the PBE function with HSE06 hybrid function [20]. The Boltzmann transport equation within the rigid band and constant relaxation approximation in the BOLTZTRAP2 [21] program are used to calculate the electronic transport properties. Supercell of $2 \times 2 \times 1$ is used in the calculations of second and third order interaction force constants. The harmonic second-order and inharmonic third-order interaction force constants are calculated in the finite displacement method [22]. The phonon dispersion curves are calculated in the PHONOPY [23]. Based on the Boltzmann transport equation, the phonon transport properties are calculated in the SHENGBTE code [24]. The three phonon scattering channels are calculated according to the study of Yang [25]. The bonding states are analyzed by calculating the crystal orbital Hamilton populations (COHP) and the integrated crystal orbital Hamilton populations (ICOHP) to the Fermi level using the LOBSTER package [26].

The carrier lifetimes $\tau$ are an important part of the input parameters in BOLTZTRAP2. The precise $\tau$ is calculated according to the electron-phonon (el-ph) scattering rates around the valence band maximum (VBM) and conduction band minimum (CBM). The EPW code is employed to calculate the $g_{mn,v}(\mathbf{k},\mathbf{q})$, as implemented in the QUANTUM ESPRESSO package [27]. The DFT calculations for the Wannier-Fourier interpolations are carried out within a uniform **k**-point mesh of $8 \times 8 \times 8$. The dynamic matrices are calculated with a **q**-point mesh of $4 \times 4 \times 4$. In EPW calculations, the interpolated **k**-point grid and **q**-point grid of $40 \times 40 \times 40$ are applied to solve the precise $g_{mn,v}(\mathbf{k},\mathbf{q})$ [28].

## III. Results and Discussions

### 1. Crystal structure

The family of II-I-V (II = Cu, Sr, Ba, I = Cu, Ag, Au, and V = As, Sb, Bi) has the same crystal structure of BaAgSb
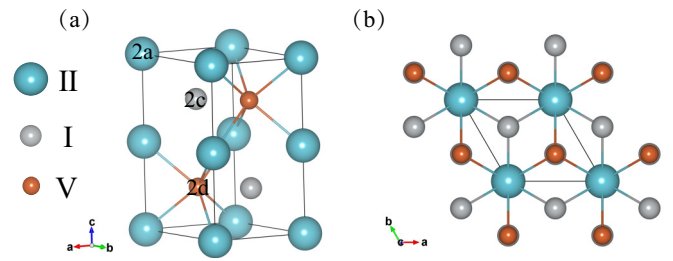


FIG. 1. Crystal structure of II-I-V from side and top view. The blue, gray, and brown spheres represent II, I, and V, respectively.

[29] (space group of $P6_3/mmc$); I and V arrange alternatively in the voids between the II layer with hexagonal close packing (hcp), as shown in Fig. 1. II, I, and V occupy $2a$ (0,0,0), $2c$ (1/3, 2/3, 1/4 ), and $2d$ (1/3, 2/3, 3/4) Wyckoff positions, respectively. The crystals with electronic band gap and real frequency phonon dispersion curves are selected and nine of them (CaCuAs, CaCuSb, BaCuAs, BaCuBi, BaAgBi, BaAgSb, SrCuSb, SrAgAs, and SrAgSb) fulfill our criteria. The lattice constants are optimized using PBE exchange correlation functions, as listed in Table I. The layer distance (c) and crystal constant (a) are increased with the atomic radius. The mass densities of nine compounds are calculated and listed in Table I. CaCuAs possesses the shortest lattice constant and less mass density. BaCuBi possesses the longest lattice constants, but BaAgBi is the densest material, which may exhibit the softest vibration modes.

The mechanical stability and thermodynamical stability are investigated. The elastic constants are calculated to study the mechanical stability, as demonstrated in Table I. The tensile strain is in the range of $-0.5\%$–$0.5\%$ with a resolution of $0.1\%$. The criteria of mechanical stability to the hexagonal crystal are $C_{11} > 0$, $C_{44} > 0$, $C_{11} > C_{12}$, and $(C_{11} + C_{12})C_{33} - 2C_{13}^2 > 0$ [30]. All the materials manifest mechanical stability. The elastic constants reflect the incompressibility of materials. $C_{11}$ and $C_{22}$ are larger than $C_{33}$, suggesting loose atomic bonds along the $c$ axis rather than in the $ab$ plane. The bulk modulus $K$ reflects the average bond strength [31]. BaAgBi with the smallest $K$ possesses loose atomic bonds, which induce the flat phonon dispersion curves of BaAgBi, as demonstrated in Fig. 4. The thermodynamical stability is estimated by using *ab initio* molecular dynamic simulations (AIMD) [32]. $NVT$ ensemble (constant volume and temperature) is used in our AIMD simulations and the time interval is 10 ps. The equilibrium evolution of Gibbs free energy demonstrates that II-I-V are stable at 300 K, 500 K, and 800 K, as shown in Supplemental Material Fig. S1 [33]. The crystal structures are also checked during the simulations to emphasize the structures reach equilibrium.

### 2. Phonon dispersion and transportation

As phonon dominates thermal transportation, analyzing the phonon dispersion curves and phonon transportation will illustrate fundamental thermal transport properties. The partial phonon density of states (PhDOS) shows the distribution of atomic vibrations, as plotted in Supplemental Material Figs. S5–S13 [33]. Usually, the heaviest elements dominate

TABLE I. Mass density $\rho$ (g cm$^{-3}$), crystal constants a and c, electronic band gap $\Delta E$ (eV), Debye temperature $\Theta_D$ (K), bulk modulus $K$ (GPa), Young's modulus $E$ (GPa), and elastic constants $C_{ij}$.

| Compounds | $\rho$ | a | c | $\Delta E$ | $\Theta_D$ | $K$ | $E$ | $C_{11}$ | $C_{12}$ | $C_{33}$ | $C_{13}$ | $C_{44}$ |
|---|---|---|---|---|---|---|---|---|---|---|---|---|
| CaCuAs | 4.89 | 4.20 | 7.96 | 0.74 | 364.50 | 68.80 | 112.93 | 163.02 | 47.78 | 84.25 | 28.33 | 35.31 |
| CaCuSb | 5.28 | 4.47 | 8.20 | 0.50 | 304.98 | 58.28 | 39.38 | 144.21 | 36.39 | 62.22 | 25.22 | 29.20 |
| BaCuAs | 5.95 | 4.34 | 9.28 | 0.23 | 318.29 | 51.60 | 121.76 | 137.56 | −15.47 | 72.891 | 36.835 | 50.96 |
| BaCuBi | 7.18 | 4.77 | 9.64 | 0.09 | 193.42 | 39.55 | 61.84 | 82.06 | 25.717 | 53.14 | 21.81 | 23.62 |
| BaAgBi | 7.81 | 4.94 | 9.13 | 0.04 | 197.29 | 46.23 | 29.08 | 102.46 | 34.317 | 50.11 | 23.11 | 26.58 |
| BaAgSb | 6.22 | 4.91 | 9.39 | 0.54 | 205.16 | 38.24 | 61.75 | 84.68 | 25.78 | 49.02 | 28.55 | 22.06 |
| SrCuSb | 5.72 | 4.54 | 8.88 | 0.52 | 311.96 | 51.74 | 112.20 | 145.41 | 8.48 | 64.41 | 23.38 | 38.94 |
| SrAgAs | 5.84 | 4.57 | 8.47 | 0.25 | 264.45 | 51.74 | 83.76 | 122.41 | 35.68 | 63.13 | 21.59 | 25.25 |
| SrAgSb | 6.05 | 4.81 | 8.18 | 0.65 | 221.56 | 46.23 | 66.11 | 99.95 | 43.24 | 52.92 | 19.20 | 22.79 |

the acoustic branches and the lightest elements dominate the high-frequency optical phonon, but the phonon distribution is different in II-I-V. For example, Bi as the heaviest element in BaAgBi dominates the acoustic modes, but it still contributes high frequency phonon with Ag, as shown in Supplemental Material Fig. S9 [33]. After analyzing all nine materials, we find that high frequency optical branches are almost devoted to the I and V sites.

To elucidate the unusual phonon vibration modes in II-I-V, the electron localization functions (ELF) are calculated. The ELF of BaAgBi along the (110) plane and the surface of ELF = 0.27 are displayed in Fig. 2. The nearly zero ELF around Ba indicates the ionic bonding of Ba and AgBi form covalent bonding for the ELF is 0.27 between them. II-I-V compounds are basically ionic with weak covalency [34], which will exhibit a high electrical conductivity and Seebeck coefficient. Covalent bonding between the Ag and Bi atoms demonstrates the relatively strong atomic bonds, which will produce intense vibrations. The 3D surface with ELF = 0.27



FIG. 2. Electron localization functions (ELF) of BaAgBi along the (110) plane (a) and 3D distribution of ELF = 0.27. The ELF values range from 0 to 1, which represents the completely delocalized and full localized electron. (e),(f) The crystal orbital Hamilton population (COHP) analysis for the nearest-neighbor cation-anion pairs in the unit cell of BaAgBi and SrCuSb.

is scattered around Ag and Bi and connected along the *ab* plane, indicating the strong covalent bonding along the *ab* plane.

The COHP analysis for different chemical bonds is performed to evaluate the chemical bonding and bond strength from another side. A larger value of COHP below the Fermi level indicates stronger bonding interaction and a smaller value means the interaction is weaker [35]. The COHPs between different pairs of nearest-neighbor atoms are plotted, as shown in Figs. 2(c) and 2(d), which shows that the interaction between the I and V atoms is the strongest, and II interact relatively weakly with the anions; hence they are weakly bonded to the lattice. The ICOHP values are calculated to evaluate the bonding environment. In BaAgBi, the ICOHP value between Bi-Ag, Bi-Ba, and Ag-Ba is −0.92, −0.35, and −0.13, respectively. It seems that the ICOHP value of Bi-Ag is larger than the other two values. In SrCuSb, the ICOHP value is −0.09785, −0.0039, and −0.00025 for Cu-Sb, Sb-Sr, and Cu-Sr, respectively. Cu-Sb has a higher ICOHP value than the other two couples. The hybridization between the I-$d$ and V-$p$ orbitals forms $p$-$d$ antibonding states below the Fermi level and it would naturally destabilize the I-V bond strength. The occupation of the $d$-$p$ antibonding states is expected to weaken the I-V bond strength. The different bonding types will produce the anisotropic atomic vibrations, corresponding to the anisotropic thermal transport properties. Ba forms rattling modes in the AgBi skeleton, suppressing the collective vibration of the crystal and hindering heat transportation in the host cages [34]. The atomic bonds between Ag and Bi along the $c$ axis are longer than that in the *ab* plane, which forms a soft bond and moderate phonon vibration along the $c$ axis. The high-frequency optical modes are almost contributed by the I-V skeleton for the weak covalent bonding between them. Thus chemical adjustments on the I-V sites can control the cutoff frequency.

The calculated $\kappa_{lat}$ is summarized in Fig. 3. II-I-V with mixing of covalent bonding and ionic bonding have anisotropic $\kappa_{lat}$. It is clear that $\kappa_{lat}$ is lower along the $c$ axis than that in the *ab* plane, which is consistent with the soft ionic bonding and longer I-V bonds along the $c$ axis. The $\kappa_{lat}$ along the $c$ axis at 300 K and 800 K are listed in Table I. The $\kappa_{lat}$ of II-I-V at 800 K is <1, indicating promising thermoelectric applications. In order to clarify the microscopic mechanism of low thermal conductivity in II-I-V, phonon transport properties are analyzed.
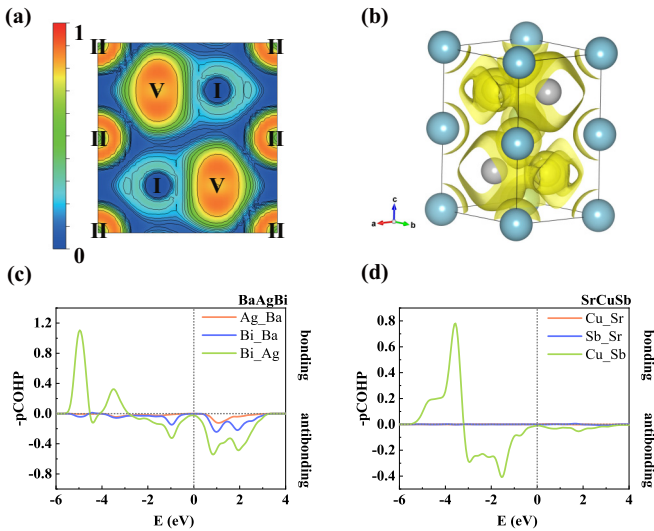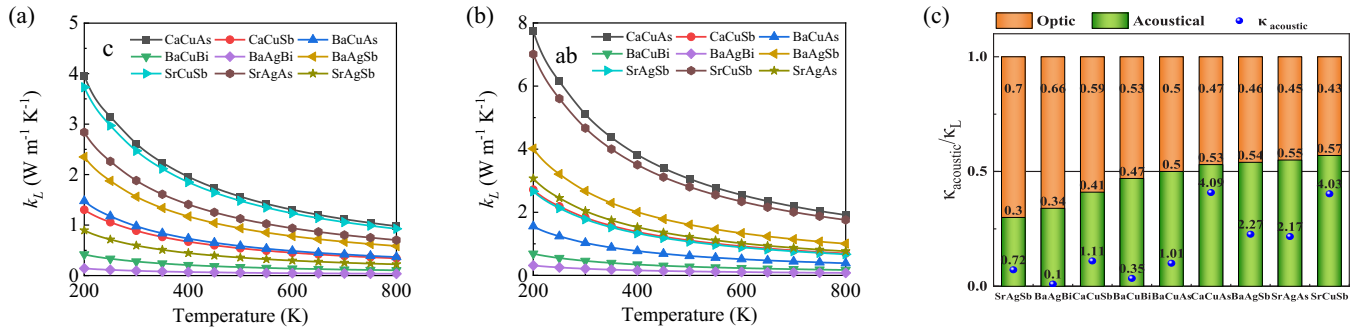
FIG. 3. Lattice thermal conductivity of II-I-V along the $c$ axis and $ab$ plane, respectively. (c) The contribution of acoustic branches on the total thermoelectric conductivity.

The acoustic phonon transportation dominates the thermal conductivity. Analyzing acoustic branches is significant to understanding the low $\kappa_{lat}$ in II-I-V. The cutoff frequencies of acoustic branches ($\omega_{max}$) are selected to describe the vibration intensity, as listed in Table II. The small $\omega_{max}$ (<1.6 THz) corresponds to the flat acoustic branches. BaAgBi possesses the smallest $\omega_{max}$ and thus the softest acoustic phonon dispersion curves and the lowest $\kappa_{lat}$ of 0.1 W m$^{-1}$ K$^{-1}$ at 300 K. CaCuAs has the highest $\omega_{max}$ and the $\kappa_{lat}$ (2.61 W m$^{-1}$ K$^{-1}$ at 300 K) is also higher than other II-I-V compounds. So, the cutoff frequency can describe the phonon softening intuitively. Research has shown that phonon softening combines with reducing the contribution of the acoustic phonon, significantly lowering the $\kappa_{lat}$ of Mg$_2$Si [36]. The contribution of acoustic and optical phonons on the $\kappa_{lat}$ are calculated, as demonstrated in Fig. 3(c). The acoustic part of $\kappa_{lat}$ in CaCuAs is 4.09 W m$^{-1}$ K$^{-1}$ at 300 K, accounting for 53% of the total $\kappa_{lat}$. When suppressing the acoustic phonon cutoff frequency by using heavy elements, the contribution of acoustic phonon decreases to 34% at room temperature and the $\kappa_{lat}$ is 0.1 W m$^{-1}$ K$^{-1}$ in BaAgBi. II-I-V with a small acoustic part of $\kappa_{lat}$ have low $\kappa_{lat}$, which is similar to Mg$_2$Si [36], inferring the soft acoustic branches also play a significant role in suppressing the thermal transportation in II-I-V. The low-frequency optical mode and the

longitude acoustic branch is generated along the $A$–$L$–$H$–$A$ direction, but we have less knowledge about the impact of acoustic-optical phonon degeneration on the phonon-phonon interaction.

The average group velocity, average transverse group velocity, and average longitude group velocity are calculated in VASPKIT [30], as displayed in Table II. II-I-V has low sound velocities (2.0–3.5 km s$^{-1}$), which are almost near that of AgSnSbSe$_3$ (2.1 km s$^{-1}$) [37]. BaAgBi has the lowest average phonon group velocities in our II-I-V compounds. CaCuAs has the highest cutoff frequency and phonon group velocities; the acoustic sound velocities ($\upsilon_{ac}$) are also relatively higher than other II-I-V compounds. The phonon branches with the group velocity demonstrate the phonon softening intuitively, as plotted in Fig. 4. The acoustic phonon velocities of CaCuSb are bigger than that of BaAgBi, which is consistent with the $\kappa_{lat}$ of CaCuSb being higher than that of BaAgBi. The phonon near the $\Gamma$ points dominates the thermal transport properties and BaAgBi possesses soft optical branches near the $\Gamma$ points. $\Gamma$–$A$ is along the $c$ axis and the evolution of the phonon dispersion curves along $\Gamma$–$A$ will influence the $\kappa_{lat}$ along the $c$ axis. $\Gamma$–$K/M$ is in the (001) plane. Analyzing the phonon dispersion curves along the $\Gamma$–$K/M$ direction will help us to understand $\kappa_{lat}$ in the $ab$ plane. The obvious different group velocities along the $\Gamma$–$K/M$ and $\Gamma$–$A$ directions confirm the anisotropic phonon transport properties. The acoustic phonon dispersion curves along $\Gamma$–$A$ have a smaller phonon group velocity than that along $\Gamma$–$K/M$, which is consistent with the low $\kappa_{lat}$ along the $c$ axis.

The phonon band gap is thought to influence the phonon interaction [38]. BaAgBi has the flattest phonon dispersion curves and smallest phonon group velocities, but exists as an optical phonon band gap. The optical phonon band gap will influence the scattering between low-frequency acoustic phonon and high-frequency optical phonon. The high-frequency optical phonon is mainly contributed by the IV skeleton; doping at these sites may eliminate the optical band gap and enhance the phonon scattering. The phonon scattering space, phonon relaxation time, and Grüneisen parameter are calculated to illustrate the intense phonon-phonon scattering, as illustrated in Supplemental Material Figs. S14–S22. BaCuBi and SrAgSb possess negative expansion properties, as they have a negative Grüneisen parameter.

TABLE II. Lattice thermal conductivity $\kappa_{lat}$ at 300 K and 800 K along the $c$ axis, Grüneisen parameter $\gamma$, average acoustic sound velocity $\upsilon$ (km s$^{-1}$), transverse sound velocity $\upsilon_T$ (km s$^{-1}$), longitude sound velocity $\upsilon_L$ (km s$^{-1}$), and the maximum acoustic frequency $\omega_m$ (THz).

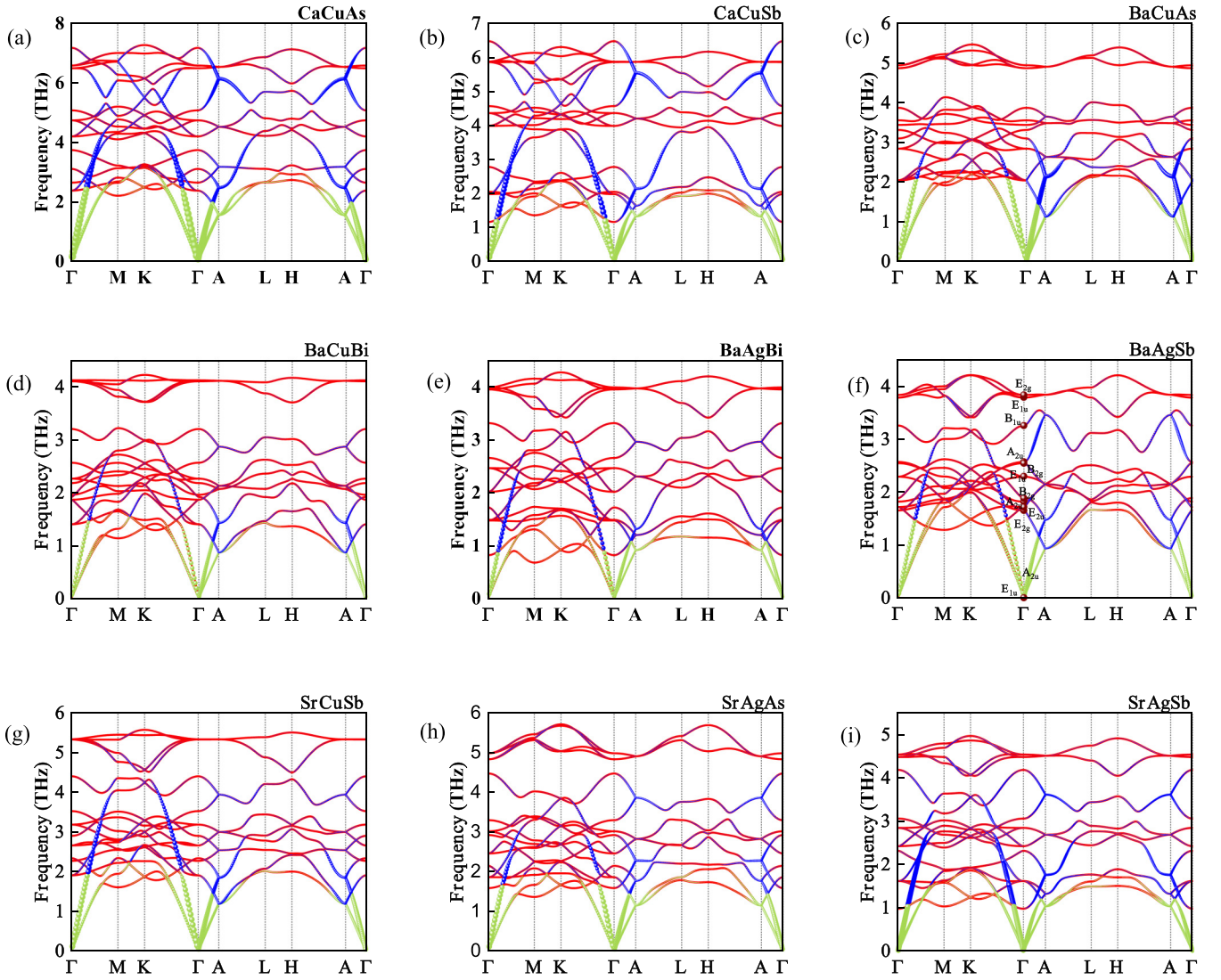| Compounds | $\kappa_{lat}^{300\ K}$ | $\kappa_{lat}^{800\ K}$ | $\gamma$ | $\upsilon$ | $\upsilon_T$ | $\upsilon_L$ | $\omega_m$ |
|---|---|---|---|---|---|---|---|
| CaCuAs | 2.61 | 0.98 | 1.41 | 3.34 | 5.04 | 3.01 | 3.14 |
| CaCuSb | 0.89 | 0.34 | 1.76 | 2.94 | 4.42 | 2.66 | 2.35 |
| BaCuAs | 0.99 | 0.37 | 1.39 | 3.15 | 4.43 | 2.87 | 2.32 |
| BaCuBi | 0.28 | 0.1 | 1.22 | 2.05 | 3.16 | 1.85 | 1.70 |
| BaAgBi | 0.1 | 0.04 | 2.16 | 2.11 | 1.90 | 3.22 | 1.56 |
| BaAgSb | 1.56 | 0.59 | 1.40 | 2.20 | 3.34 | 1.99 | 1.99 |
| SrCuSb | 2.47 | 0.92 | 1.42 | 3.12 | 4.40 | 2.84 | 2.42 |
| SrAgAs | 1.88 | 0.77 | 1.59 | 2.62 | 3.97 | 2.37 | 2.09 |
| SrAgSb | 0.6 | 0.22 | 1.35 | 2.29 | 3.57 | 2.01 | 1.86 |

FIG. 4. Phonon dispersion curves with indication of phonon group velocity. The red lines are phonon branches. The blue and green bubble represents the group velocities of optical branches and acoustic branches. The size of the bubble is proportional to the group velocity.

### 3. Three phonon scattering channels

The geometric structure plays a decisive role in determining the phonon scattering channels, so that the phonon symmetry is analyzed to uncover the intense phonon-phonon scattering from the aspect of scattering channels. The phonon band symmetry is analyzed according to the irreducible representations. II-I-V have six double-degeneracy and six nondegeneracy phonon branches at the $\Gamma$ points, as demonstrated in Fig. 4(f). However, the six and four degenerated phonon branches appear at $A$ points, which are not produced by the crystal symmetry. At the first Brillouin zone, the high-symmetry points $A$, $K$, $L$, $H$, and $M$ have the points space of $D_{6h}$, $D_{3h}$, $C_{2v}$, $D_{3h}$, and $D_{2h}$, respectively. The three-phonon scattering pathways are calculated by the following formula:

$$\langle q\xi \otimes q'\xi' \otimes q''\xi''^* | 1\rangle = \sum_{\{R\}} \chi^{q\xi}(\{R\})\chi^{q'\xi'}(\{R\})\chi^{q''\xi''}(\{R\})^*$$
$$\times \Delta(q + q' - q''). \quad (1)$$

$\chi^{q\xi}$ is the character of the irreducible representation. The condition of a forbidden phonon absorption or emission process is as follows:

$$\langle q\xi \otimes q'\xi' \otimes q''\xi''^* | 1\rangle = 0. \quad (2)$$

According to Eq. (2), three phonon scattering channels along the high-symmetry path in the first Brillouin zone are listed in Table III. The existence of numerous phonon scattering pathways indicates the possible intense three phonon scattering of II-I-V. II-I-V has more three phonon scattering channels than $Ba_2AgSb$ [39].

### 4. Electronic structure and electronic transport

The electronic band structures are shown in Fig. 5. All these compounds have electronic band gaps in 0–1 eV and the valence band maximum (VBM) is located at the $\Gamma$ point. Due to the crystal symmetry, two valence bands converge at the $\Gamma$ point, which increases the carrier concentration under $p$-type doping and deduces the promising $p$-type performance
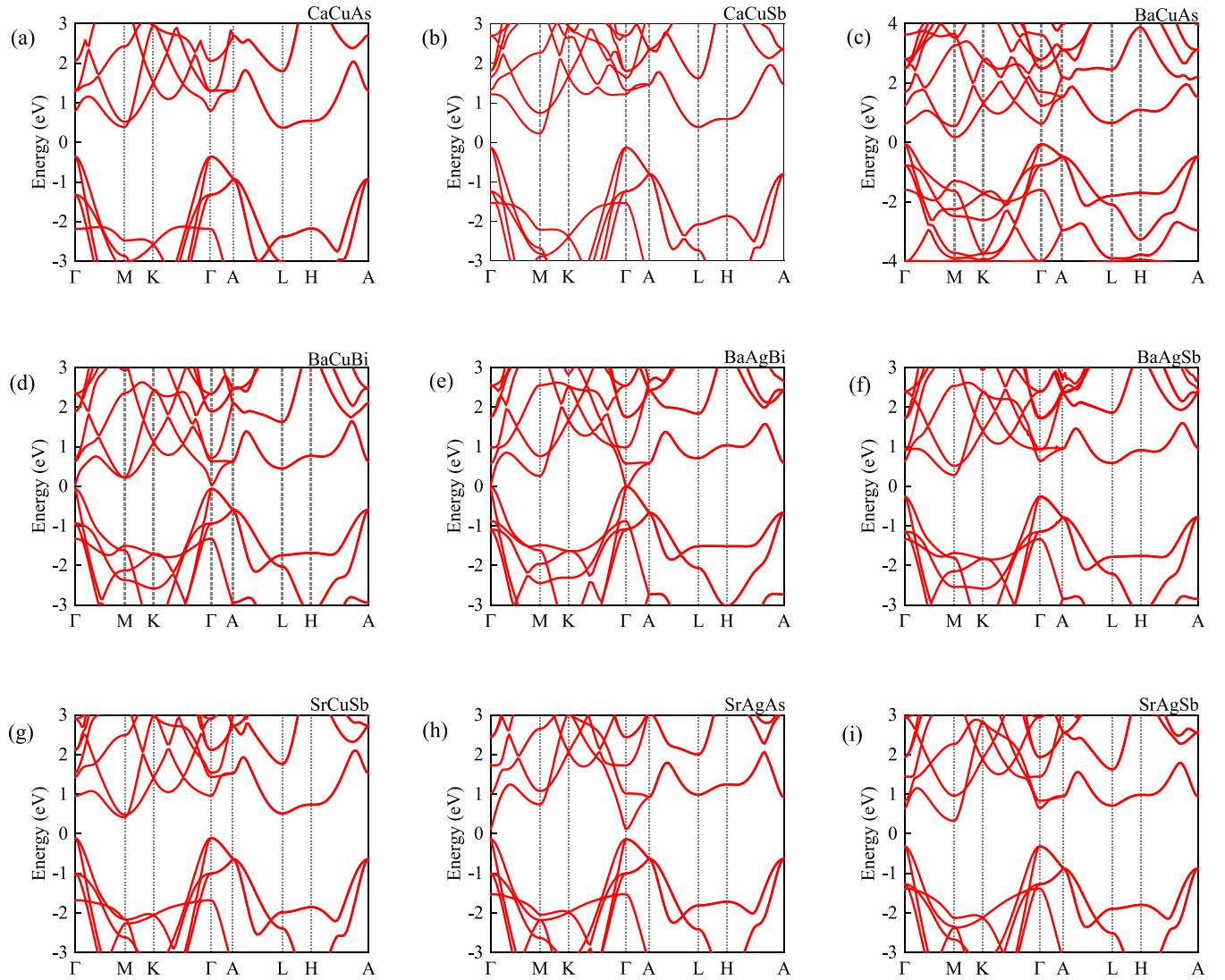
FIG. 5. Electronic band structures of II-I-V.

in Zintl-phase compounds [14]. BaAgBi, BaCuBi, and SrAgAs have direct electronic band gap for the CBM located at the $\Gamma$ points. Other materials have indirect electronic band gap for the CBM near the $M$ points. SrCuSb has two conductive

TABLE III. Symmetry based three-phonon scattering channels.

| High symmetry path | Three-phonon scattering channels | | |
|---|---|---|---|
| $\Gamma \rightarrow M(D_{2h})$ | $A_g A_g A_g$ | $A_g A_u A_u$ | $A_g B_{3u} B_{3u}$ |
| | $A_g B_{1g} B_{1g}$ | $A_g B_{1u} B_{1u}$ | $A_u B_{1g} B_{1u}$ |
| | $A_g B_{3g} B_{3g}$ | $A_g B_{2u} B_{2u}$ | $B_{1g} B_{2u} B_{3u}$ |
| | $A_u B_{3g} B_{3u}$ | $B_{3g} B_{1u} B_{2u}$ | |
| $\Gamma \rightarrow A(D_{6h})$ | $E_{2g} E_{2g} E_{2g}$ | $B_{2g} A_{2u} B_{1u}$ | $E_{2g} B_{1u} E_{1u}$ |
| | $E_{2g} E_{1u} E_{1u}$ | $B_{2g} E_{1u} E_{2u}$ | |
| | $E_{2g} E_{2u} E_{2u}$ | $E_{2g} A_{2u} E_{2u}$ | |
| $\Gamma \rightarrow L(C_{2v})$ | $A_1 A_1 A_1$ | $A_1 B_1 B_1$ | $A_2 B_1 B_2$ |
| | $A_1 A_2 A_2$ | $A_1 B_2 B_2$ | |
| $\Gamma \rightarrow K/H(D_{3h})$ | $E' E' E'$ | $A_2'' E' E''$ | |
| | $E' E'' E''$ | $A_1'' E' E''$ | |

bands converged at the CBM and directly benefits electronic conductivity by enhancing carrier concentration [10]. The second conductive bands of CaCuAs and BaCuBi are near the CBM; it is easy to participate in the conductivity under proper doping. The chemical composition has a great influence on the conductive bands. The Bader charge analysis shows that II denotes one electron to V and half electrons to I and this is consistent with the ionic bonding between II and I-V skeleton. The electronic density of states are calculated as demonstrated in Supplemental Material Figs. S5–S13 [33]. The conduction band has primarily II $d$ character and this is consistent with II devoting electrons with normally filled $p$ orbitals. The weak hybridization between V $p$ and I $d$ electrons contributes to the valence band. The electrons of II are localized, so they hardly occupy the valence band.

The electronic band masses are calculated as displayed in Supplemental Material Table S1 [33]. The upper valence band and bottom conductive band show anisotropic band masses. For the VBM of II-I-V located at the $\Gamma$ point, the hole effective masses near the $\Gamma$ point are calculated. The upper valence band is heavier along the $\Gamma$–$A$ line ($c$ axis) than that along the
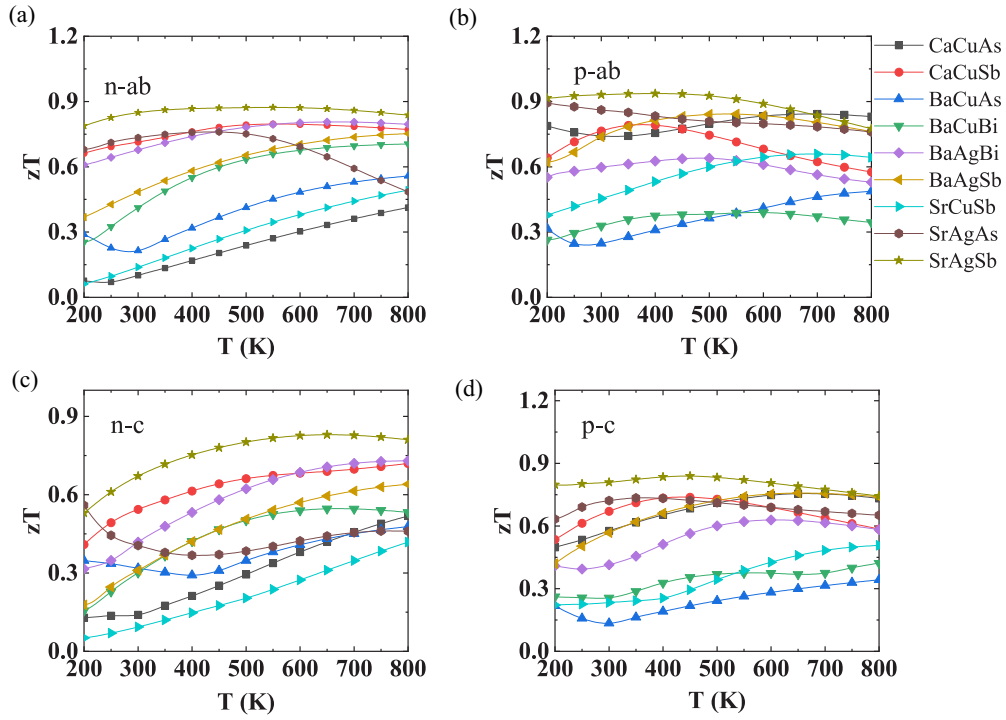
FIG. 6. TE performance calculated by the electronic transport properties. $zT$ along the *ab* plane and *c* axis under *n*-type (a) and *p*-type (b) doping and $zT$ along the *c* axis under *n*-type (c) and *p*-type (d) doping, respectively.

$\Gamma$–$K$ line (*ab* plane). The mixture of light bands is favorable for carrier mobility and heavy bands lead to a higher Seebeck coefficient [40], which is beneficial to the thermoelectric performance [41]. The electron and hole mobility are calculated. Our materials possess high carrier mobility with anisotropic behavior. The hole mobility is higher than the electron mobility and this is consistent with the higher electron effective mass. Both the hole mobility and electron mobility in the *c* axis are higher than that along the *ab* plane, inferring the high electrical conductivity along the *c* axis and high Seebeck coefficient in the *ab* plane.

The electronic transport properties are simulated using the rigid band and relaxation time approximation, as implemented in the BOLTZTRAP2 [21]. The carrier scattering times are needed to calculate the electronic transport properties; both the constant relaxation time and relaxation times calculated according to the electron-phonon interaction are used in our calculations. The evolution of the Seebeck coefficient ($S$), electrical conductivity ($\sigma$), and electronic thermal conductivity ($\kappa_e$) with carrier concentration are demonstrated in Supplemental Material Figs. S23 and S24 [33]. The flat bands produce high Seebeck coefficient and very low mobility, but the low effective mass is beneficial to the thermoelectric performance [40]. The differences between the *ab* plane and *c* directions show the anisotropic electron transport properties. The evolutions of $S$ with temperature under a specific carrier concentration are shown in Supplemental Material Fig. S23 [33]. $S$ decreased with carrier concentration and increased with temperature. II-I-V are high Seebeck effect materials with a large $S$. The Seebeck coefficient is higher in the *ab* plane than along the *c* axis, which is consistent with the weak covalent bonding along the *ab* plane. CaCuAs has the largest Seebeck coefficient. II-I-V materials have higher

thermovoltage along the *ab* plane, except for CaCuAs, CaCuSb, and BaAgSb, which have higher Seebeck effects along the *c* axis. The electrical conductivity with the temperature is shown in Supplemental Material Fig. S24 [33]. BaAgBi has the largest electrical conductivity under *n*-type doping. BaCuBi has the most considerable hole conductivity under *p*-type doping. BaAgBi and BaCuBi with a small electronic band gap have high electrical conductivity. Both $\sigma$ and $\kappa_e$ are

TABLE IV. Seebeck coefficient ($S$), maximum $zT$ calculated by the epw relaxation time, and corresponding absolute temperature along *ab* direction.

| Compounds | Doping | $S$ | $zT_{max}$ | Temperature |
|---|---|---|---|---|
| CaCuAs | *n* | 219.16 | 0.41 | 800 |
|  | *p* | 374.74 | 0.84 | 650 |
| CaCuSb | *n* | 349.06 | 0.80 | 550 |
|  | *p* | 328.37 | 0.79 | 350 |
| BaCuAs | *n* | 228.12 | 0.56 | 800 |
|  | *p* | 179.18 | 0.49 | 800 |
| BaCuBi | *n* | 264.75 | 0.70 | 800 |
|  | *p* | 146.91 | 0.40 | 550 |
| BaAgBi | *n* | 333.80 | 0.81 | 650 |
|  | *p* | 258.90 | 0.64 | 500 |
| BaAgSb | *n* | 329.35 | 0.75 | 800 |
|  | *p* | 365.55 | 0.84 | 550 |
| SrCuSb | *n* | 233.87 | 0.49 | 800 |
|  | *p* | 262.45 | 0.66 | 650 |
| SrAgAs | *n* | 247.70 | 0.76 | 450 |
|  | *p* | 329.99 | 0.89 | 200 |
| SrAgSb | *n* | 393.47 | 0.87 | 550 |
|  | *p* | 470.85 | 0.94 | 400 |

TABLE V. Seebeck coefficient ($S$), maximum $zT$ calculated by the epw relaxation time, and corresponding absolute temperature along $c$ axis.

| Compounds | Doping | $S$ | $zT_{max}$ | Temperature |
|---|---|---|---|---|
| CaCuAs | $n$ | 230.03 | 0.51 | 800 |
|  | $p$ | 311.34 | 0.75 | 650 |
| CaCuSb | $n$ | 340.52 | 0.72 | 800 |
|  | $p$ | 320.79 | 0.74 | 450 |
| BaCuAs | $n$ | 201.48 | 0.48 | 800 |
|  | $p$ | 124.52 | 0.34 | 800 |
| BaCuBi | $n$ | 210.79 | 0.55 | 650 |
|  | $p$ | 137.35 | 0.42 | 800 |
| BaAgBi | $n$ | 264.15 | 0.73 | 800 |
|  | $p$ | 235.59 | 0.63 | 600 |
| BaAgSb | $n$ | 268.61 | 0.64 | 800 |
|  | $p$ | 304.97 | 0.76 | 650 |
| SrCuSb | $n$ | 226.00 | 0.42 | 800 |
|  | $p$ | 201.86 | 0.51 | 800 |
| SrAgAs | $n$ | 165.497 | 0.46 | 750 |
|  | $p$ | 383.915 | 0.73 | 350 |
| SrAgSb | $n$ | 374.23 | 0.83 | 650 |
|  | $p$ | 416.88 | 0.84 | 450 |

increased with doping concentration, as more carriers participate in the electronic and thermal transportation.

**5. Figure of merit**

Different from our former calculations [29], which used the deformation potential theory, the carrier lifetimes are calculated based on the electron-phonon interaction. The calculated thermoelectric figure of merit with temperature and carrier concentration is shown in Fig. 6. The maximum $zT$, the corresponding $S$, and absolute temperature are listed in Tables IV and V. II-I-V is high-performance thermoelectric material with high $zT$ (0.41–0.94) and large $S$ (>200 μV K$^{-1}$). The comparison with other reported materials are listed in Supplemental Material Table S3 [33], which includes Refs. [11,42–46]. $S$ influence thermoelectric performance and materials with higher $S$ show high thermoelectric performance. SrAgSb with high $S$ and low thermal conductivity show the high thermoelectric $zT$ of 0.94 at 400 K. SrAgSb possesses the highest thermoelectric efficiency along the $c$ axis under $p$-type doping. BaAgBi and BaCuBi are $n$-type thermoelectric materials for the higher $p$-type thermoelectric performance.

The $\kappa_{lat}$ of BaAgBi and BaCuBi is lower than that of SrAgSb for the intense phonon scattering. From our previous analysis, Sb hardly occupies the conductive band and V sites decide the cutoff frequency, so doping heavy elements (Bi) at the Sb sites may enhance the phonon scattering and suppress the thermal transport in SrAgSb, which will further improve the thermoelectric efficiency.

**IV. CONCLUSIONS**

Our first principles calculations proposed nine Zintl-phase compounds II-I-V (II = Cu, Sr, Ba, I = Cu, Ag, Au, and V = As, Sb, Bi) with anisotropic electronic and thermal transport properties. II-I-V with eight-valence electrons in $P6_3/mmc$ symmetry are mechanically, thermodynamically, and dynamically stable semiconductors with a desirable figure of merit ($\sim$1). The bonding properties, electronic, and thermal transport properties show some regularities in II-I-V. II forms rattling modes in the I-V skeleton, enhancing acoustic and optical phonon iteration. I-V plays an essential role in suppressing the high frequent vibrations, deducing soft vibration modes. The heaviest elements produce soft acoustic branches and suppress the contribution of the acoustic phonon on the thermal conductivity, which also lowers the total thermal conductivity. In the valence band, V $p$ and I $d$ electron hybridization forms a $p$-$d$ antibonding state, weakening the I-V bonding. The II $d$ electron occupies the conductive band and II forms ionic bonding with others. The I-V skeleton leads to the coexistence of high dispersion and flat band edge near the VBM, which ensures the coexistence of high $\sigma$ and $S$. The mixing of ionic bonding and weak covalent bonding in II-I-V leads to high carrier mobilities and intrinsically ultralow lattice thermal conductivity. The symmetry-based three-phonon scattering pathways demonstrate the possible intense phonon-phonon scattering. This study uncovered the regularities in $P6_3/mmc$ Zintl-phase materials and may be helpful for further study in experiments.

[1] C. Gayner and K. K. Kar, Recent advances in thermoelectric materials, Prog. Mater. Sci. **83**, 330 (2016).

[2] S. Hao, L. Ward, Z. Luo, V. Ozolins, V. P. Dravid, M. G. Kanatzidis, and C. Wolverton, Design strategy for high-performance thermoelectric materials: The prediction of electron-doped KZrCuSe$_3$, Chem. Mater. **31**, 3018 (2019).

[3] G. J. Snyder and E. S. Toberer, Complex thermoelectric materials, in *Materials for Sustainable Energy: A Collection of Peer-Reviewed Research and Review Articles from Nature Publishing Group* (World Scientific, Singapore, 2011), pp. 101–110.

[4] C. Wang, C. Zheng, and G. Gao, Bulk and monolayer ZrS$_3$ as promising anisotropic thermoelectric materials: A comparative study, J. Phys. Chem. C **124**, 6536 (2020).

[5] C.-M. Lin, W.-C. Chen, and C.-C. Chen, First-principles study of strain effect on thermoelectric properties of LaP and LaAs, Phys. Chem. Chem. Phys. **23**, 18189 (2021).

[6] T. Pandey, A. S. Nissimagoudar, A. Mishra, and A. K. Singh, Ultralow thermal conductivity and high thermoelectric figure of merit in mixed valence $In_5X_5Br$ (X = S, and Se) compounds, J. Mater. Chem. A **8**, 13812 (2020).

[7] S. M. Kauzlarich, S. R. Brown, and G. J. Snyder, Zintl phases for thermoelectric devices, Dalton Trans. **2007**, 2099 (2007).

[8] K. Jia, C.-L. Yang, M.-S. Wang, and X.-G. Ma, High thermoelectric figure of merit and thermopower of $HfTe_5$ at room temperature, J. Phys.: Condens. Matter **32**, 345501 (2020).

[9] L. Zhang, M.-H. Du, and D. J. Singh, Zintl-phase compounds with $SnSb_4$ tetrahedral anions: Electronic structure and thermoelectric properties, Phys. Rev. B **81**, 075117 (2010).

[10] J. Park, Y. Xia, and V. Ozoliņš, High thermoelectric power factor and efficiency from a highly dispersive band in $Ba_2BiAu$, Phys. Rev. Appl. **11**, 014058 (2019).

[11] T. Zhou, Z. Feng, J. Mao, J. Jiang, H. Zhu, D. J. Singh, C. Wang, and Z. Ren, Thermoelectric properties of Zintl phase $YbMg_2Sb_2$, Chem. Mater. **32**, 776 (2020).

[12] T. Zhou, J. Song, X. Lei, Q. Zhang, J. Bi, D. Gao, J. Jiang, and C. Wang, Achieving $n$-type conduction in $YbMg_2Sb_2$-based compounds through defect engineering and doping, Acta Mater. **223**, 117467 (2022).

[13] C. Chen, Z. Feng, H. Yao, F. Cao, B.-H. Lei, Y. Wang, Y. Chen, D. J. Singh, and Q. Zhang, Intrinsic nanostructure induced ultralow thermal conductivity yields enhanced thermoelectric performance in Zintl phase $Eu_2ZnSb_2$, Nat. Commun. **12**, 5718 (2021).

[14] P. Gorai, A. Ganose, A. Faghaninia, A. Jain, and V. Stevanović, Computational discovery of promising new $n$-type dopable ABX Zintl thermoelectric materials, Mater. Horizons **7**, 1809 (2020).

[15] K. Guo, Q.-G. Cao, X.-J. Feng, M.-B. Tang, H.-H. Chen, X. Guo, L. Chen, Y. Grin, and J.-T. Zhao, Enhanced thermoelectric figure of merit of Zintl phase $YbCd_{2-x}Mn_xSb_2$ by chemical substitution, Eur. J. Inorg. Chem. **2011**, 4043 (2011).

[16] Vikram, B. Sahni, C. K. Barman, and A. Alam, Accelerated discovery of new 8-electron half-Heusler compounds as promising energy and topological quantum materials, J. Phys. Chem. C **123**, 7074 (2019).

[17] G. Kresse and J. Furthmüller, Efficient iterative schemes for ab initio total-energy calculations using a plane-wave basis set, Phys. Rev. B **54**, 11169 (1996).

[18] P. E. Blöchl, Projector augmented-wave method, Phys. Rev. B **50**, 17953 (1994).

[19] J. P. Perdew, K. Burke, and M. Ernzerhof, Generalized gradient approximation made simple, Phys. Rev. Lett. **77**, 3865 (1996).

[20] J. Heyd, G. E. Scuseria, and M. Ernzerhof, Hybrid functionals based on a screened Coulomb potential, J. Chem. Phys. **118**, 8207 (2003).

[21] G. K. Madsen and D. J. Singh, BoltzTraP. A code for calculating band-structure dependent quantities, Comput. Phys. Commun. **175**, 67 (2006).

[22] S. Baroni, S. De Gironcoli, A. Dal Corso, and P. Giannozzi, Phonons and related crystal properties from density-functional perturbation theory, Rev. Mod. Phys. **73**, 515 (2001).

[23] A. Togo and I. Tanaka, First principles phonon calculations in materials science, Scr. Mater. **108**, 1 (2015).

[24] W. Li, J. Carrete, N. A. Katcho, and N. Mingo, ShengBTE: A solver of the Boltzmann transport equation for phonons, Comput. Phys. Commun. **185**, 1747 (2014).

[25] R. Yang, S. Yue, Y. Quan, and B. Liao, Crystal symmetry based selection rules for anharmonic phonon-phonon scattering from a group theory formalism, Phys. Rev. B **103**, 184302 (2021).

[26] S. Maintz, V. L. Deringer, A. L. Tchougréeff, and R. Dronskowski, LOBSTER: A tool to extract chemical bonding from plane-wave based DFT, J. Comput. Chem. **37**, 1030 (2016).

[27] P. Giannozzi, S. Baroni, N. Bonini, M. Calandra, R. Car, C. Cavazzoni, D. Ceresoli, G. L. Chiarotti, M. Cococcioni, I. Dabo *et al.*, QUANTUM ESPRESSO: A modular and open-source software project for quantum simulations of materials, J. Phys.: Condens. Matter **21**, 395502 (2009).

[28] S. Poncé, E. R. Margine, C. Verdi, and F. Giustino, EPW: Electron–phonon coupling, transport and superconducting properties using maximally localized Wannier functions, Comput. Phys. Commun. **209**, 116 (2016).

[29] S.-F. Wang, Z.-G. Zhang, B.-T. Wang, J.-R. Zhang, and F.-W. Wang, Zintl phase BaAgSb: Low thermal conductivity and high performance thermoelectric material in *ab initio* calculation, Chin. Phys. Lett. **38**, 046301 (2021).

[30] V. Wang, N. Xu, J.-C. Liu, G. Tang, and W.-T. Geng, Vaspkit: A user-friendly interface facilitating high-throughput computing and analysis using VASP code, Comput. Phys. Commun. **267**, 108033 (2021).

[31] M. Wang, C. Xia, Y. Wu, D. Z. Chen, Z. Chen, N. heng Ma, and H. wei Wang, Phase stability, elastic and electronic properties of Hf-Rh intermetallic compounds from first-principles calculations, RSC Adv. **7**, 20241 (2017).

[32] J. Hafner, *Ab-initio* simulations of materials using VASP: Density-functional theory and beyond, J. Comput. Chem. **29**, 2044 (2008).

[33] See Supplemental Material at http://link.aps.org/supplemental/10.1103/PhysRevB.108.235213 for the detail about the ab initio molecular dynamic simulations, phonon dispersion curves, electronic band structures, electronic density of states, electronic transport property, three phonon scattering properties such as group velocity, phase space, relaxation time, Gruneisen parameter, carrier lifetime, and the testing of parameters.

[34] Z. Feng, Y. Fu, Y. Yan, Y. Zhang, and D. J. Singh, Zintl chemistry leading to ultralow thermal conductivity, semiconducting behavior, and high thermoelectric performance of hexagonal KBaBi, Phys. Rev. B **103**, 224101 (2021).

[35] K. Pal, Y. Xia, J. He, and C. Wolverton, High thermoelectric performance in $BaAgYTe_3$ via low lattice thermal conductivity induced by bonding heterogeneity, Phys. Rev. Mater. **3**, 085402 (2019).

[36] X. Tan, G. Liu, H. Shao, J. Xu, B. Yu, H. Jiang, and J. Jiang, Acoustic phonon softening and reduced thermal conductivity in $Mg_2Si_{1-x}Sn_x$ solid solutions, Appl. Phys. Lett. **110**, 143903 (2017).

[37] Y. Luo, S. Hao, S. Cai, T. J. Slade, Z. Z. Luo, V. P. Dravid, C. Wolverton, Q. Yan, and M. G. Kanatzidis, High thermoelectric performance in the new cubic semiconductor $AgSnSbSe_3$ by high-entropy engineering, J. Am. Chem. Soc. **142**, 15187 (2020).

[38] N. Wang, M. Li, H. Xiao, X. Zu, and L. Qiao, Layered LaCuOSe: A promising anisotropic thermoelectric material, Phys. Rev. Appl. **13**, 024038 (2020).

[39] S.-F. Wang, Z.-G. Zhang, B.-T. Wang, J.-R. Zhang, and F.-W. Wang, Intrinsic ultralow lattice thermal conductivity in the

full-Heusler compound $Ba_2AgSb$, Phys. Rev. Appl. **17**, 034023 (2022).

[40] Y. Pei, H. Wang, and G. J. Snyder, Band engineering of thermoelectric materials, Adv. Mater. **24**, 6125 (2012).

[41] S. K. Saha and G. Dutta, Elastic and thermal properties of the layered thermoelectrics BiOCuSe and LaOCuSe, Phys. Rev. B **94**, 125209 (2016).

[42] C. Chen, W. Xue, S. Li, Z. Zhang, X. Li, X. Wang, Y. Liu, J. Sui, X. Liu, F. Cao *et al.*, Zintl-phase $Eu_2ZnSb_2$: A promising thermoelectric material with ultralow thermal conductivity, Proc. Natl. Acad. Sci. USA **116**, 2831 (2019).

[43] N. Guechi, A. Bouhemadou, Y. Medkour, Y. Al-Douri, R. Khenata, and S. Bin-Omran, Electronic and thermoelectric properties of the layered Zintl phase $CaIn_2P_2$: First-principles calculations, Philos. Mag. **100**, 3023 (2020).

[44] D. Behera, R. Sharma, H. Ullah, H. S. Waheed, and S. Mukherjee, Electronic, optical, and thermoelectric investigations of Zintl phase $AAg_2Se_2$ (A = Sr, Ba) compounds: A first-principle approach, J. Solid State Chem. **312**, 123259 (2022).

[45] L. Borgsmiller, Q. Li, M. Y. Toriyama, and G. J. Snyder, New Zintl Phase $Yb_{10}MgSb_9$ with high thermoelectric performance, Adv. Energy Mater. **13**, 2300393 (2023).

[46] U. Aydemir, A. Zevalkink, A. Ormeci, S. Bux, and G. J. Snyder, Enhanced thermoelectric properties of the Zintl phase $BaGa_2Sb_2$ via doping with Na or K, J. Mater. Chem. A **4**, 1867 (2016).